Monthly Notices
of the
ROYAL ASTRONOMICAL SOCIETY

MNRAS **462,** S210–S219 (2016)
Advance Access publication 2016 October 4

doi:10.1093/mnras/stw2529

67P/C-G inner coma dust properties from 2.2 au inbound to 2.0 au outbound to the Sun

V. Della Corte,[1⋆] A. Rotundi,[1,2⋆] M. Fulle,[3] S. Ivanovski,[1] S. F. Green,[4] F. J. M. Rietmeijer,[5] L. Colangeli,[6] P. Palumbo,[1,2] R. Sordini,[1,2] M. Ferrari,[1] M. Accolla,[7] V. Zakharov,[8] E. Mazzotta Epifani,[9] P. Weissman,[10] E. Gruen,[11] J. J. Lopez-Moreno,[12] J. Rodriguez,[12] E. Bussoletti,[2] J. F. Crifo,[13] F. Esposito,[14] P. L. Lamy,[15] J. A. M. McDonnell,[4,16,17] V. Mennella,[14] A. Molina,[18] R. Morales,[12] F. Moreno,[12] E. Palomba,[1] J. M. Perrin,[15,19] R. Rodrigo,[20,21] J. C. Zarnecki,[21] M. Cosi,[22] F. Giovane,[23] B. Gustafson,[24] J. L. Ortiz,[12] J. M. Jeronimo,[12] M. R. Leese,[4] M. Herranz,[12] V. Liuzzi[2] and A. C. Lopez-Jimenez[12]

Affiliations are listed at the end of the paper

Accepted 2016 October 3. Received 2016 September 30; in original form 2016 July 8; Editorial Decision 2016 September 30

ABSTRACT

GIADA (Grain Impact Analyzer and Dust Accumulator) on-board the *Rosetta* space probe is designed to measure the momentum, mass and speed of individual dust particles escaping the nucleus of comet 67P/Churyumov–Gerasimenko (hereafter 67P). From 2014 August to 2016 June, *Rosetta* escorted comet 67P during its journey around the Sun. Here, we focus on GIADA data taken between 2015 January and 2016 February which included 67P's perihelion passage. To better understand cometary activity and more specifically the presence of dust structures in cometary comae, we mapped the spatial distribution of dust density in 67P's coma. In this manner, we could track the evolution of high-density regions of coma dust and their connections with nucleus illumination conditions, namely tracking 67P's seasons. We also studied the link between dust particle speeds and their masses with respect to heliocentric distance, i.e. the level of cometary activity. This allowed us to derive a global and a local correlation of the dust particles' speed distribution with respect to the H_2O production rate.

Key words: instrumentation: detectors – methods: data analysis – comets: general – comets: individual: 67P/Churyumov–Gerasimenko.

1 INTRODUCTION

The *Giotto* space probe at Comet Halley imaged dust features dominating the inner coma, which were restricted to the subsolar hemisphere (Keller et al. 1986). *In situ* observations performed during the *Giotto* flyby of comet Grigg–Skjellerup coupled with models suggest that dust structures are present in its innermost coma (McBride et al. 1997).

For the first time, the Grain Impact Analyser and Dust Accumulator (GIADA) instrument on-board *Rosetta* (Della Corte et al. 2014) was able to monitor dust-rich areas present in the coma of comet 67P/Churyumov–Gerasimenko (hereafter 67P) in much greater detail. GIADA could do better for a two reasons: (1) due to *Rosetta's* trajectory, essentially matched to that of the comet, long-term monitoring of the comet's activity was possible for the very first time; (2) for the first time a dust instrument measured mass, speed, cross-section and the exact detection time/position of individual dust particles simultaneously. GIADA was able to (1) characterize 67P's dust environment (Fulle et al. 2015); (2) monitor the dust loss rate and the particle mass distribution at the surface of the sunlit nucleus; (3) monitor the dust mass distribution of 67P as it evolved with time (Rotundi et al. 2015; Fulle et al. 2016); and (4) in the case of dust detected along closely bound orbits, provide a hint of the region of the nucleus from where the dust originated (Della Corte et al. 2015). Even when 67P's coma dust structures are studied by *in situ* measurements combined with ground-based observations, understanding their formation mechanisms and connecting them to specific active areas on the nucleus is a very challenging process. Large-scale dust coma structures observed from the ground are modelled as the result of multiple small features arising from

⋆ E-mail: vincenzo.dellacorte@iaps.inaf.it (VDC); rotundi@uniparthenope.it (AR)

one region (Vincent et al. 2013; Lara et al. 2015). By analysing the images taken by the Optical, Spectroscopic, and Infrared Remote Imaging System camera (Keller et al. 2007) on-board *Rosetta*, Lara et al. (2015) reach the conclusion that large-scale dust structures are likely to be due to the contribution of many small features. Jet-like features present in 67P's coma were studied by Lin et al. (2016), who concluded that curved jets form as a combination of specific dust particle sizes (0.1–1 mm) and the activity coming from equatorial regions; larger dust particles are accelerated to lower radial velocities than smaller ones. Vincent et al. (2015) monitored and modelled the 'fuzzy collimated streams of cometary material arising from the nucleus' of 67P, proposing that active cliffs are their main source. But what exactly is a jet, or a jet-like feature? Is it a single peculiar feature connected to a specific limited active area due to chemical heterogeneity? Or is it rather the normal cometary activity coming from an extended area more active because of surface topography? Crifo et al. (2002) and Zakharov et al. (2009) demonstrate, by means of ab-initio physical models, that coma dust structures can be induced by nucleus asphericity and focused on gas flows due to local topography. Topological diversity can create physical conditions, such as higher temperatures, which will affect the sublimation of different volatiles, explaining the spatial correlation between the high rate of dust ejection and of H_2O sublimation (Della Corte et al. 2015; Migliorini et al. 2016). Thus, what could be interpreted as a chemical heterogeneity-driving factor for activity would actually be attributable to a topographic one. Coma dust distribution reconstruction by means of *in situ* dust detections contributes to the study of cometary activity and to the processes driving the formation of specific dust structures in cometary comae. In this paper, we present efforts made to identify high dust density areas in the coma of 67P, which can contribute to the trace-back models aimed at providing information on the areas where the activity originates, thus contributing to the study of the dust ejection process.

2 OBSERVATIONS

From 2014 August to 2016 September, *Rosetta* followed comet 67P along its orbit from 3.7 au inbound to perihelion and outbound to 4.0 au. We here focus on GIADA data acquired from 2015 January to 2016 February, i.e. when 67P was at 2.2 au before perihelion, to perihelion at 1.24 au and to 2.00 au outbound. Due to spacecraft safety concerns, e.g. star tracker performance, the trajectories were mostly constrained to large nucleus distances (>100 km) and high phase angles (the angle Sun – 67P – *Rosetta*), i.e. outside dust-rich areas as observed by Della Corte et al. (2015). Despite these operational limitations, GIADA was able to monitor efficiently 67P's dust environment and its evolution, determining detection time, mass and speed for individual dust particles. We divided the observations into four different periods characterized by different dust environment behaviours. The first period includes the flybys and lasted from 2015 January 22 to March 31 (Period 1). The second is the pre-perihelion period from 2015 April 14 to June 30 (Period 2). Perihelion, occurring on 2015 August 13, is included in the third period from 2015 July 1 to October 31 (Period 3). The post-perihelion phase starts on 2015 November 1 and continues until the 2016 February 22 (Period 4). In the time frame considered here, *Rosetta* only followed trajectories that included distances from the nucleus surface of less than 30 km during the first period (Fig. 2). In the following, we report dust particle detections together with the observation geometry in the comet body-fixed reference frame (Preusker et al. 2015, Cheops reference frame).

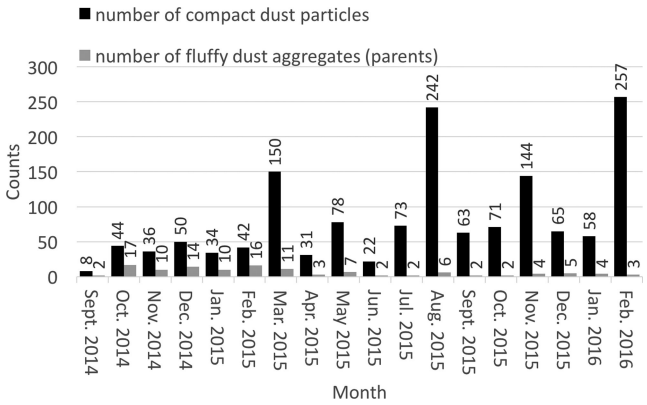

Figure 1. On the *y*-axis, we report the counts of compact particles (GDS + IS and IS-only detections) compared with the number of parent fluffy aggregates (long-lasting sequence of GDS-only detections; Fulle et al. 2015) grouped for each month of the mission (*x*-axis) detected by GIADA from 2014 September to 2016 February. Compact particles dominate, especially in the period under consideration in this study (2015 January–2016 February). 67P's perihelion occurred on 2015 August 13.

GIADA detections are classified according to which the GIADA subsystem detects the individual particle entering the instrument. For easier comprehension, we present here a brief summary of the detection and particle types, described in detail by Della Corte et al. (2015). GIADA detects individual dust particles in the following combinations: (1) only with the Grain Detection System (GDS), i.e. a laser curtain plus photodiodes (GDS-only detection); (2) only with the Impact Sensor (IS), i.e. a plate connected to piezoelectric sensors (IS-only detection); (3) both GDS and IS subsystems detect the particle (GDS + IS detection). Coupled GDS + IS detections provide individual particle mass, speed and geometrical cross-section by means of calibration (Della Corte et al. 2016) obtained with cometary dust analogues (Ferrari et al. 2014). GDS-only detections provide particles' geometrical cross-section and speed, while IS-only detections provide particle momentum. Since the subsystem response depends on the particle physical characteristics (size, optical properties and density) we classified the different types of detection as different classes of particles. GDS-only detections occur as isolated events or as 'dust showers', i.e. up to hundreds of detections in tens of seconds, and correspond to fluffy low-density (<1 kg m^{-3}) aggregates (Fulle et al. 2015). The GDS-only detections are explained as portions of parent particles fragmented by the internal electrostatic tension caused by charging from the secondary electron flux from *Rosetta* (Fulle et al. 2015). IS-only and GDS + IS detections are of compact particles with a density of (1.9 ± 1.1) × 10^3 kg m^{-3} (Rotundi et al. 2015), the only difference being the particle cross-section (i.e. IS-only particles are too small to be detected by the GDS subsystem; Della Corte et al. 2015). Although the number of fluffy fragments is larger than that of compact particles, the number of fluffy aggregates (parents) is negligible with respect to the compact particles throughout the *Rosetta* mission, but especially in the period under analysis (2015 January–2016 February). This can be seen in Fig. 1 where we include the bound orbit period (2014 September–2015 January) detections for comparison. In particular, the ratio between compact particles and fluffy parents jumps from about 3 in the bound orbit phase to ≥10 for the period under study. In addition, 67P's coma brightness contribution from fluffy aggregates is less than 15 per cent (Fulle et al. 2015). This is the reason why we focus our attention on compact particles, i.e. on the IS-only and GDS + IS detections, in this study. In Table 1,

Table 1. Number of compact particles per observation period using GDS + IS and IS-only detections. For each period, we provide the range of speeds and masses measured by GDS + IS detections, and the range of momenta measured by IS-only and GDS + IS detections.

Observation period	Number of IS-only	Number of GDS + IS	Speed (GDS + IS) range (m s^{-1})	Mass (GDS+IS) range (kg)	Momentum (kg m s^{-1})
1	160	54	0.3–16.9	3.2×10^{-9}–3.4×10^{-7}	2.7×10^{-8}–1.4×10^{-6}
2	104	21	3.73–17.5	8.2×10^{-9}–1.4×10^{-6}	5.2×10^{-8}–1.9×10^{-5}
3	433	23	1.2–34.8	2.8×10^{-9}–7.4×10^{-7}	4.5×10^{-8}–1.9×10^{-5}
4	477	43	0.6–25.5	4.6×10^{-9}–1.2×10^{-6}	4.2×10^{-8}–1.8×10^{-5}

we report the number of detected compact particles together with the range of momenta measured by GIADA for the different periods considered, and the mass and speed ranges for the GDS + IS detections. In the following sections, we analyse the dust detection rates with respect to the observation geometry for the four identified periods. The first expected parameter influencing the number of particles detected is the distance from the nucleus: the closer the spacecraft the higher the number of detections. However, the dominant factor is the difference in activity driven by comet season, with the most active subspacecraft point latitudes moving from the Northern to the Southern hemisphere passing through the equinox. In Period 1, the obliquity of the nucleus rotation axis (Preusker et al. 2015) sets the comet summer in the Northern hemisphere and the effects on the activity are quite evident: the maximum particle detection rate occurs when *Rosetta* is flying over northern latitudes (Fig. 2a). This effect is quite evident at the beginning of Period 1 (Fig. 2a, the first yellow arrow on the left) when the distance of the spacecraft from the nucleus is constant: the detections become null even at 30 km from the nucleus surface when the latitude goes down to the Southern hemisphere (about -65°). Della Corte et al. (2015) found that the illumination condition influences the dust ejection: the lower the phase angle the higher the particle detection rate.

2.1 Period 1: 2015 January–March dust particle detections

In this period, *Rosetta* performed two close and several far flybys of 67P's nucleus, with different observation geometries. The flybys were designed with different characteristics in terms of closest approach distance, phase angle, nucleus latitude and longitude at flyover. These types of trajectory optimized GIADA detections and the coma dust environment reconstruction. Fig. 2 shows dust detections, along with the *Rosetta* nucleus distance, the phase angle and the latitude of the subspacecraft point. The correlation between dust detection rate and the observation geometry is quite evident from the plot. The highest GIADA dust detection rate for this period occurred when *Rosetta* was at low phase angle, flying over high northern latitudes and at close distances from the nucleus (green arrows in Fig. 2a). On the contrary, when *Rosetta* flew over southern latitudes, even if at low phase angles and at close distances, the detection rate remained low (yellow arrows in Fig. 2a) because the Southern hemisphere regions during Period 1 were only briefly illuminated. At the end of Period 1, *Rosetta* went into safe mode due to a spacecarft 'Attitude and Orbit Control System' problem connected to the crossing of a region of high dust density which was also recorded by GIADA (the right most arrow in Fig. 2a). This event influenced the selection of the trajectory in the following period.

2.2 Period 2: 2015 April–June dust particle detections

In Period 2, the spacecraft performed a series of far flybys with closest approach distances greater than 90 km (Fig. 2b) and phase angles higher than 50° in order to avoid high dust density regions and remain within the spacecraft's safe thermal conditions. From Fig. 2b, it is also evident that in this period GIADA's high detection rate is driven by detections at low phase angles and the distance does not have a critical role. The subspacecraft latitude does not appear to affect the dust particle detections. This is due to the inclination of the comet rotation axis, the summer shifting from the Northern hemisphere to the Southern hemisphere: the activity is dispersed over all latitudes (Fig. 2b, green arrows).

2.3 Period 3: 2015 July–October dust particle detections

During the perihelion period, the comet's activity continued to rise and it was necessary to move *Rosetta* to distances >160 km from the nucleus. However, the combination of low phase angle and southern latitude induced a very high rate in dust particle detections (the red arrow in Fig. 2c) during the last week of August and the first week of September. In this period, a far excursion of the spacecraft to 1500 km was performed to study the properties of the comet plasma environment. Even at such large distances, GIADA could detect numerous dust particles (green arrow in Fig. 2c). This was due to the fact that Rosetta was flying at low phase angles (close to 50°) and over southern sub-spacecraft latitudes. During this period, GIADA detected: (1) a large number of particles at low phase angle in a quasi-continuous flow; (2) three bursts of detections each lasting about 3 h that we define as 'outbursts'.

2.4 Period 4: 2015 November–2016 February dust particle detections

After the 'far excursion', *Rosetta* reduced its distance from the nucleus and flew from the terminator to 50° phase angle (spacecraft thermal constraint limit) segments covering almost the complete half-space over the illuminated side of the nucleus (Fig. 2d). These trajectories allowed GIADA to satisfactorily describe the coma dust distribution.

3 METHODS

In order to describe 67P's inner coma dust environment, concerning both the dust spatial distribution and the dust dynamics, we analysed GIADA data with a dual approach. These focused on: (1) where the dust accumulates within the coma, i.e. using individual dust particle detection coordinates we obtain dust spatial distribution maps; (2) how the dust particles behave dynamically, i.e. studying the trend between particle speed versus mass and evaluating speeds

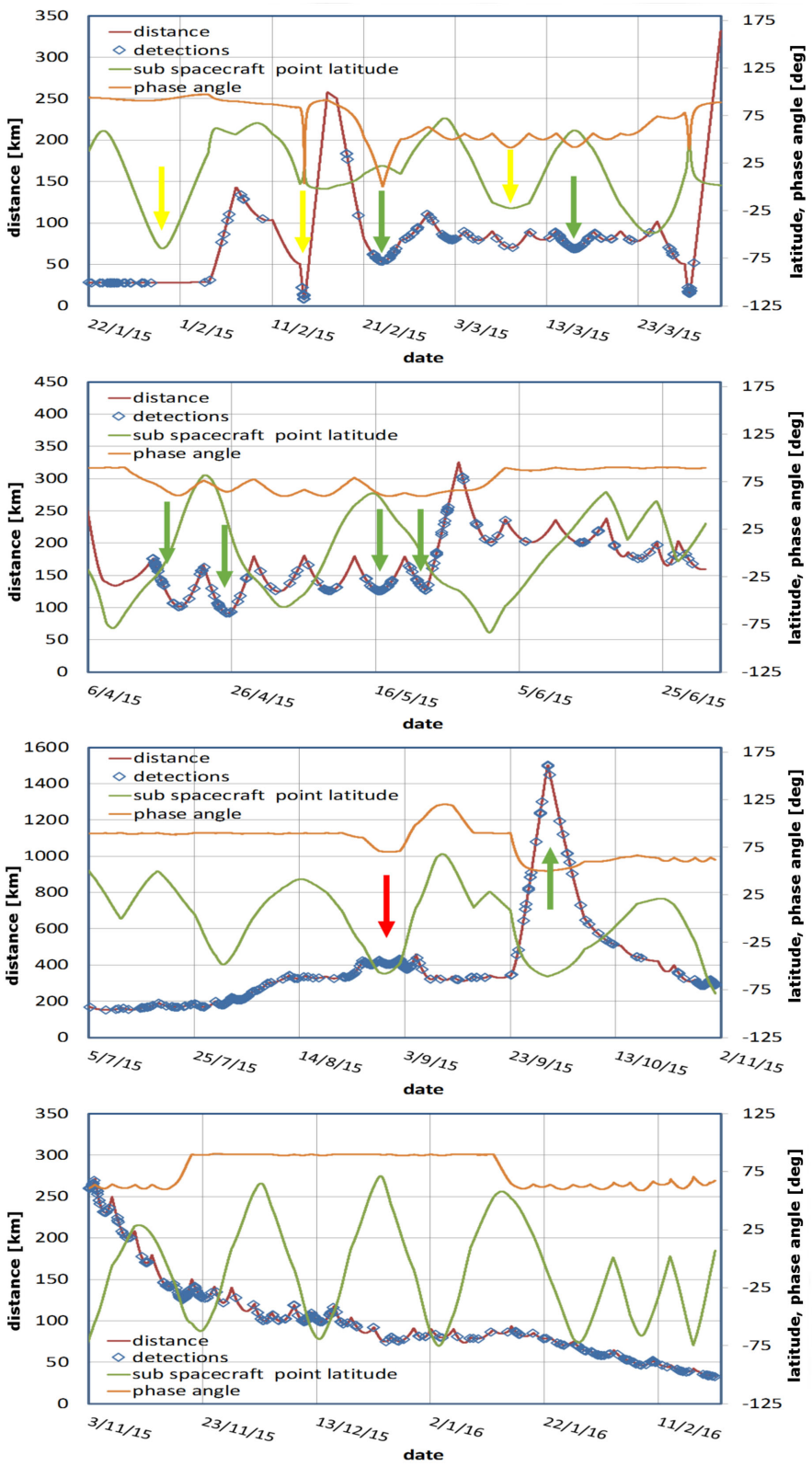

Figure 2. GIADA detections with respect to time in the body-fixed reference frame divided into the four periods under consideration: (a) Period 1, from 2015 January 22 to March 31; (b) Period 2, from 2015 April to June; (c) Period 3, from 2015 July to October; (d) Period 4, from 2015 November to 2016 February. In each plot, detections are superimposed on the *Rosetta*–nucleus distance, the phase angle and the subspacecraft latitude; see the text for explanation of the coloured arrows.

Table 2. Best-fitting values of γ and A for the mass versus speed power-law relationship ($v = Am^{\gamma}$), reported for different heliocentric distances for all the GDS + IS detections as well as, separately, for GDS–IS detections at phase angles below and above 75°.

Observation period	Heliocentric distance (AU)	A (all detections)	A (low phase angle)	A (high phase angle)	γ (low phase angle)	γ (high phase angle)
0	3.4–2.5	-1.77 ± 0.02	-1.5 ± 0.70	-2.74 ± 0.70	-0.28 ± 0.09	-0.44 ± 0.09
1	2.5–2.0	-1.57 ± 0.02	-0.96 ± 0.55	-3.71 ± 1.43	-0.24 ± 0.07	-0.57 ± 0.19
2,3	2.0–1.3[a]–1.7	-1.31 ± 0.04	-0.68 ± 1.26[b]	-2.62 ± 1.04	-0.21 ± 0.16	-0.49 ± 0.14
4	1.7–2.0	-1.57 ± 0.02	-1.06 ± 0.86	-2.66 ± 1.65	-0.25 ± 0.11	-0.47 ± 0.21

Notes. [a]Perihelion; [b]Large uncertainties are due to poor statistics.

and masses starting from particle momentum measurements (IS-only detections).

3.1 Dust spatial distribution

To reconstruct the coma dust spatial density, we report GIADA detections in the comet Centred Solar Orbital (CSO) reference frame defined as:

(i) The X-axis points from the comet to the Sun.
(ii) The Y-axis is the component of the inertially referenced Sun velocity relative to the comet and orthogonal to the X-axis.
(iii) The Z-axis is $X \times Y$, completing the right-handed reference frame.

The CSO reference frame seems more appropriate to describe the coma dust distribution, highlighting the direct link between the nucleus illumination condition and the coma dust spatial density. As the CSO reference frame rotates along the comet orbit, pointing the X-axis always towards the Sun, the comet's spin axis orientation varies accordingly (see Section 4.1 for spin axis angle values relative to the periods under study). In order to obtain maps of dust density at a normalized distance, we proceeded as follows:

(i) We applied a standard coordinate transformation from Cartesian to spherical coordinates (X, Y, Z) to (latitude, longitude, radius) in the CSO reference frame. An advantage of this transformation is also to be found in the relationship between phase angles with latitude and longitude.
(ii) We weighted each detection with the time spent by *Rosetta* at the specific phase angle.
(iii) We weighted each detection by the square of the ratio between the detection distance and the minimum 67P – *Rosetta* distance in the period under consideration.
(iv) We computed a 2D dust detection histogram as a function of spherical CSO coordinates for each of the four periods.
(v) We added, for comparison, a similar analysis performed on GIADA data acquired between 2014 August 1 and 2015 January 22, Period 0 (Della Corte et al. 2015).

3.2 Dust particles' speeds and masses

With the aim of studying the trend between the particle speed and its mass, we focused on the GDS + IS detections, which give both speed and mass for each individual dust particle. By applying the bootstrap statistical method (Efron & Tibshirani 1994) to these GIADA data, we derived values and confidence limits of the power-law index, γ, and of the parameter A, in the speed versus mass relation ($v = Am^{\gamma}$) for the periods under study. Because a low number of GDS + IS detections occurred during Periods 2 and 3, we decided to apply the bootstrap method combining these periods. The calculated γ-values are all compatible, within the uncertainties, with the values found by Della Corte et al. (2015), namely $\gamma = -0.32 \pm 0.18$. Thus, we use this value to derive the A values for the different periods (Table 2). For the sake of completeness, in Table 2, we also report the data for the first phase of the mission ('Period 0': 2014 August–2015 January). The derived A values reported in Table 2 indicate that this parameter increases with decreasing heliocentric distance, i.e. with increasing cometary activity. Since the dust production rate rises at low phase angles (see Section 2), we decided to check for a possible dependence of the speed versus mass trend with respect to the phase angle. We therefore fitted the data separating the dust particles detected at phase angles $<75°$ (Fig. 3, left-hand panels) from those at phase angles $>75°$ (Fig. 3, right-hand panels). As can be seen from Table 2 and each panel of Fig. 3, within each period there is a difference in the values determined for the parameters. In particular, the A values for low phase angle detections are always larger than those determined for high phase angles. Higher A values correspond to higher dust particle speeds. The same trend is observed for the γ parameter for each period. The determination of these parameters not only gave the possibility of looking for a connection between the speed versus mass trend and the cometary activity level (or in general to the gas production rate for which see Results and Discussion section), but also allowed us to improve GIADA data analyses. In fact, the best-fitting curves together with the calibration curves (IS signal versus momentum, p, and versus kinetic energy, K) obtained by Della Corte et al. (2016) allowed us to calculate the masses and speeds from the IS-only detections. For the IS-only detections, we can write the following equations:

$$p = mv, \tag{1}$$

$$K = (1/2)mv^2, \tag{2}$$

$$v = Am^{\gamma}. \tag{3}$$

We solved this overdetermined equation system using the least-squares method deriving the values of mass and speed for each IS-only detection. The trial-and-error system solution method converges to a solution for 95 per cent of the IS-only detections. In order to check the reliability of this method, we applied the computation to GDS + IS data for which we could derive individual particle masses by combining the momentum and speed measured by GIADA. Fig. 4 shows a comparison of the mass values retrieved by solving equations (1)– (3) with those directly determined from measurements (blue circles and red squares, respectively). We conclude that, while there is a large scatter in the distribution of mass and speed for the direct measurements, the equation system does generally produce values that cover the same mass range with speeds

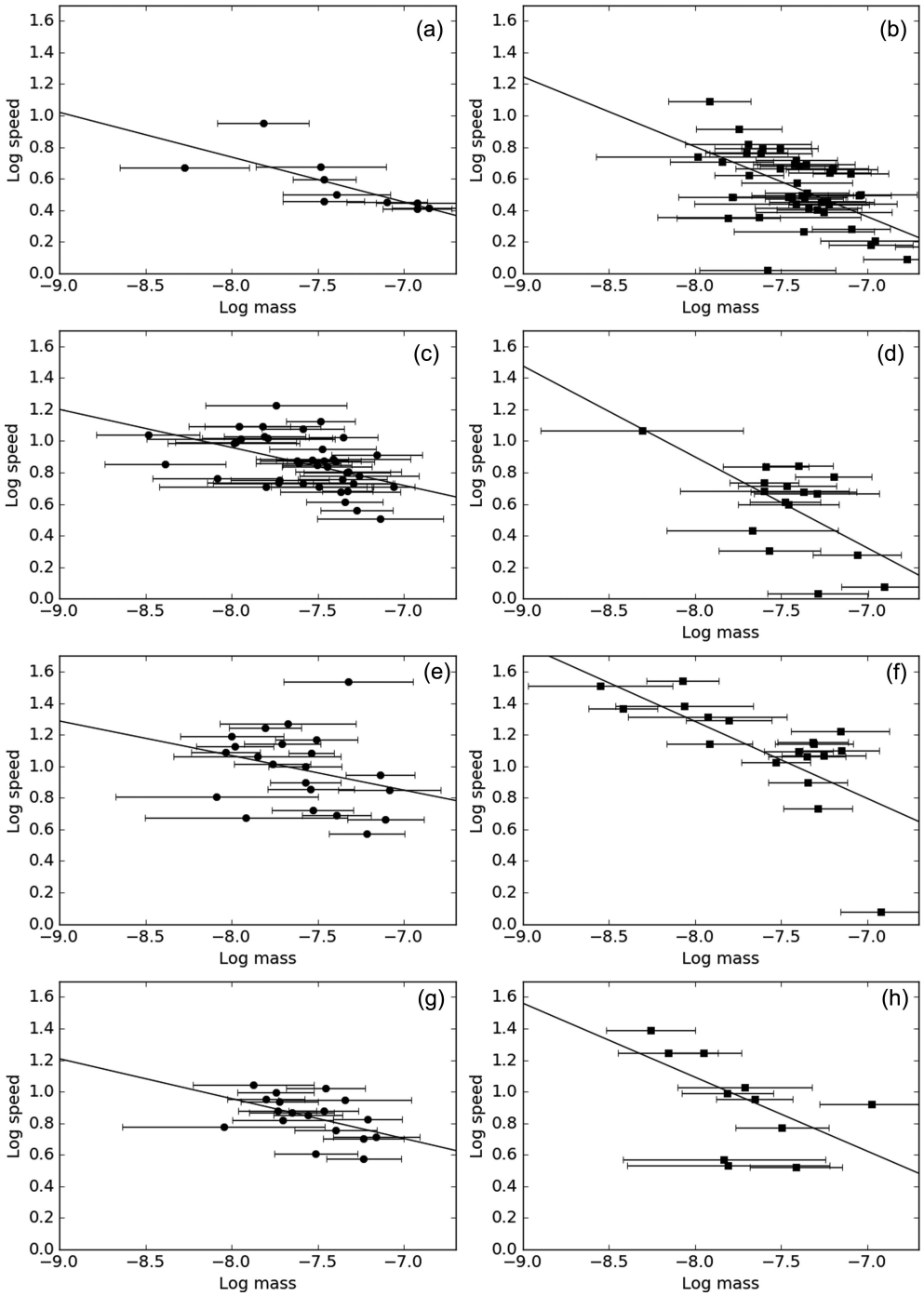

Figure 3. Speed (m s^{-1}) versus mass (kg) trend for the GDS + IS detections occurring at phase angle <75° (left-hand panels) and >75° (right-hand panels) with the respective fits for: (a) and (b) Period 0: 2014 August–2015 January; (c) and (d) Period 1: 2015 January–March; (e) and (f) Periods 2 and 3: 2015 April–October; (g) and (h) Period 4: 2015 November–2016 February. Each symbol corresponds to one particle measurement. The uncertainty in the speed measurements is 6 per cent.

representative of the true data. The exception is for the combined Periods 2 and 3 (Fig. 4c) which cover times close to perihelion when cometocentric distance, activity levels and illumination geometry of the nucleus are changing rapidly; γ values evaluated for specific phase angles should be rather considered. In addition, the masses derived by applying this method to the IS-only detections confirm the mass distribution obtained by Fulle et al. (2016) and Rotundi et al. (2015).

4 RESULTS AND DISCUSSION

4.1 Dust spatial distribution maps

During the periods under study, GIADA was continuously making measurements while pointing towards the nucleus. Thanks to GIADA's wide field of view (37°), only highly off-nadir pointing would have affected the results reported in Fig. 5 but they occurred so rarely that their effect on the overall results is negligible. In Fig. 5

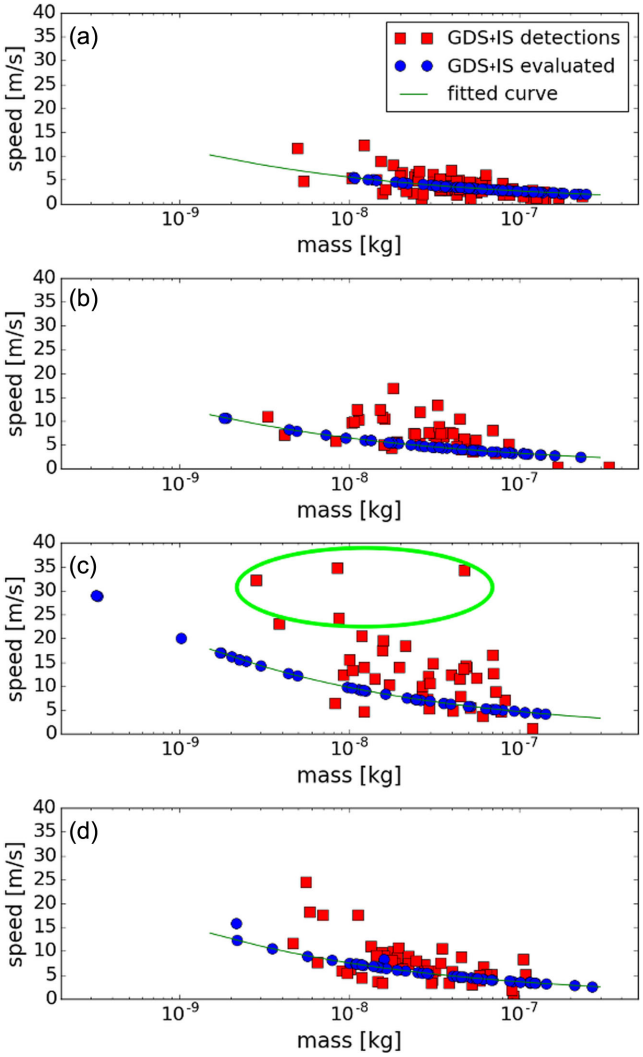

Figure 4. Masses derived for the IS-only momentum measurements plus the speeds evaluated with equations (1)– (3) (blue circles) compared with the masses measured by the GDS + IS detections (red squares): (a) Period 0: 2014 August–2015 January; (b) Period 1: 2015 January–March; (c) Periods 2 and 3: 2015 April–October; (d) Period 4: 2015 November–2016 February. The lines correspond to $v = Am^{\gamma}$, where the A values are those calculated for each specific period and reported in Table 2 and $\gamma = -0.32$.

(left-hand panels), we present GIADA detections along the *Rosetta* trajectory, without any normalization, in a Mollweide projection – the red horizontal segment indicates the track of the pointing direction of the comet's rotation axis. In Fig. 5 (right-hand panels), we present the corresponding dust spatial density maps whose sequence shows the dust spatial variation from Period 0 to Period 4. We obtained the maps (right-hand panels) from the dust detections (left-hand panels) normalized with respect to the illumination conditions and the distance from the nucleus (see Section 3.1 for details). We applied the same analysis to GIADA data acquired in Period 0 (2014 August 1–2015 January 22; Della Corte et al. 2015), for comparison (Fig. 5a). In this period, the rotation axis pointed towards the Sun, -30° to -60° longitude in the CSO spherical coordinates (the red horizontal segment indicates the track of the pointing direction of the rotation axis), exposing 67P's Northern hemisphere to illumination. Looking at the corresponding map (Fig. 5b), we find that the higher dust density coma regions are in fact in the Northern hemisphere, i.e. the areas illuminated longer each day. During Period 1 (2015 January–March), the dust spatial density map (Fig. 5d) shows a well-defined area with enhanced intensity confined between -30° and -60° longitude and 30°–60° latitude. The track of the rotation axis (the red segment in Fig. 5c) is slightly shifted in longitude with respect to the high-density area of the coma. This confirms that the longer an area is illuminated, the higher is the dust production. From 2015 April, spacecraft safety requirements imposed limitations on the phase angle ($>50^{\circ}$) preventing monitoring of the dust in these coma regions (blue areas on maps). The dust spatial density map obtained for Period 3 again shows dust density enhancements in the area identified in the previous period. New high dust density areas appear at low latitudes (Fig. 5f). During this time period, the nucleus rotation axis track crosses the terminator plane (90° meridian in Fig. 5e). Nucleus areas earlier in shadow or only partially illuminated in the Southern hemisphere start to be sunlit for longer, and the dust spatial density starts to increase in coma regions at low and southern latitudes (Fig. 5e). During Period 3, around perihelion, the direction of the rotation axis moved over a wide range of longitudes (about 90°) due to the higher 67P orbital speed. This resulted in a dust spatial density, now located at very low latitude, spread over a wide range of longitudes (Fig. 5h). At the end of this period, the spacecraft performed a far excursion reaching phase angles down to 50° and distances up to 1500 km from the nucleus. Since the maps are obtained by weighting dust detections with respect to the distance (see Section 3.1), we find a high dust density region in the Southern hemisphere even though *Rosetta* flew at very large distances from the nucleus. During Period 4, because of the decreasing comet activity, *Rosetta* followed trajectories with gradually decreasing distances to the nucleus (Fig. 2d). Getting closer while dust ejection was still high led to a spatial dust density map with the highest number of GIADA detections of the entire mission. Even though the limitation in phase angle ($>50^{\circ}$; Fig. 5i) was still in place, the trajectories allowed good coma coverage. The high dust density region remained in the Southern hemisphere, but moved towards higher latitudes and negative longitudes (Fig. 5j). An overview of the five maps shows how the coma dust spatial density distribution changes in relation to 67P's journey around the Sun. The evolution is linked to 67P's seasons induced by the inclination of the rotation axis of the nucleus (red segments in Fig. 5, left-hand panels). The seasonal effects are evidenced by the shift of the high-density areas from the Northern hemisphere from 2014 August to 2015 March to the Southern one from 2015 July to 2016 February, with 2015 April to June as the transition period. In addition, the highest dust density coma region coordinates correspond to the most illuminated nucleus areas; this suggests that the particles reaching GIADA mainly follow radial trajectories. The fact that the major fraction of the dust is emitted at low phase angles (Fig. 5, right-hand panels) confirms the results reported by Fulle et al. (2016) and Rotundi et al. (2015) who derived the dust-to-gas ratio and dust production rates using mainly the GIADA detections occurring when *Rosetta* was flying at low phase angles.

4.2 Dust particle dynamics

Dust spatial density maps suggest that the trajectory of the dust particles escaping from the nucleus during the comet's day are not far from the radial direction. This implies that particles escaping from the surface regions under specific illumination conditions are detected by GIADA when it is in the same relative geometry with respect to the Sun. Particles emitted from a nucleus region at a specific local time, i.e. Sun–zenith angle, are detected by GIADA

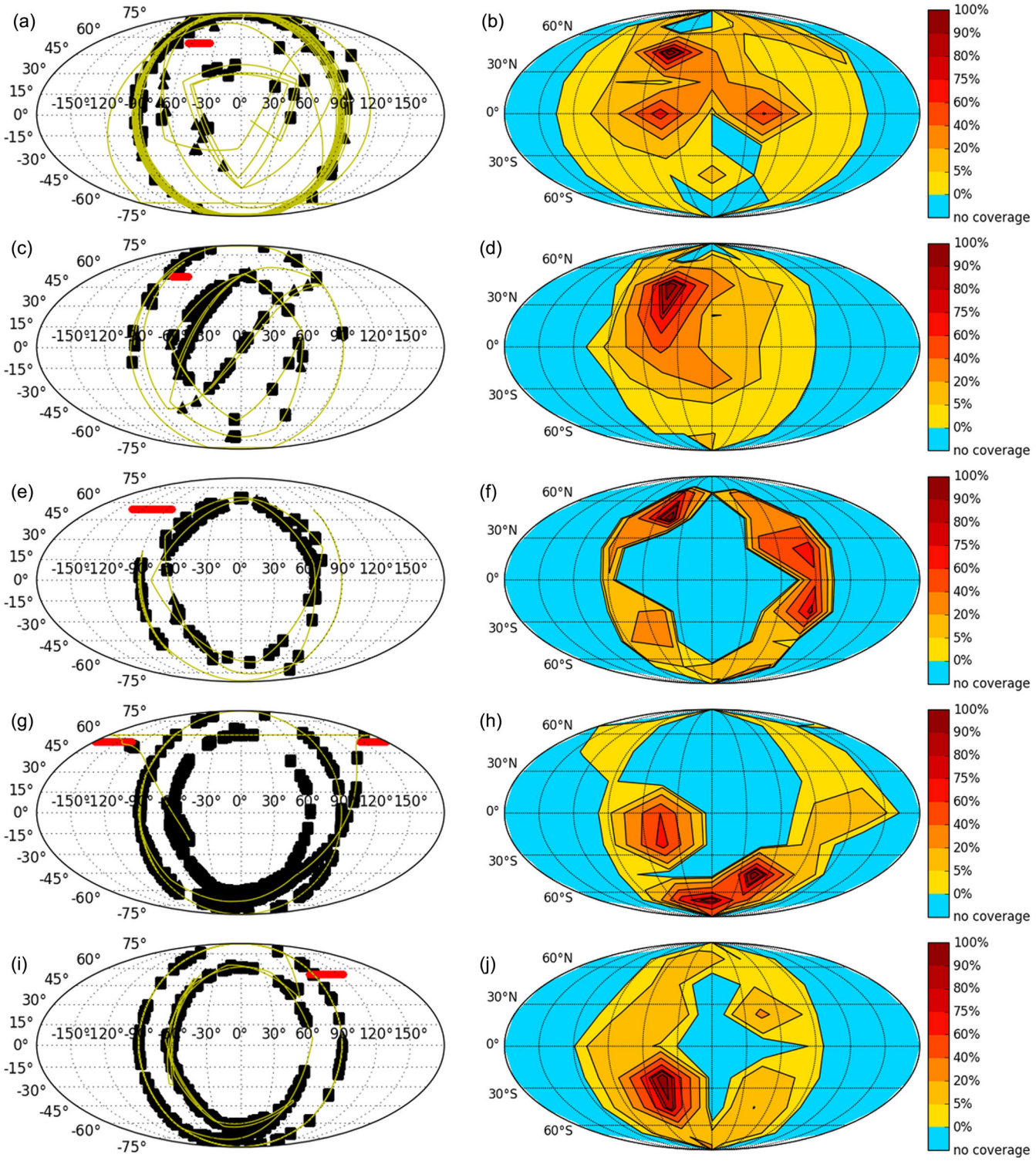

Figure 5. Dust particle detections along the *Rosetta* trajectory (left-hand panels) and dust spatial density maps (right-hand panels) in a Mollweide projection. The Mollweide projection is an equal-area, pseudocylindrical map projection in which the equator is represented as a straight horizontal line perpendicular to a central meridian one-half its length. The parallels compress near the poles; the labels to the left correspond to the latitudes. The meridians, equally spaced at the equator, at 90° east and west form a perfect circle, which in our case identifies the terminator plane; the labels across the centre correspond to the longitude. The red bars in the left-hand panels track the spin axis orientation evolution during each period. The phase angle of each detection is directly linked to its latitude and longitude. Blue areas in the maps correspond either to areas not covered or to non-detections. The first row corresponds to Period 0 (from 2014 August 1 to 2015 January 22, reported for comparison); the second row refers to Period 1; the third row refers to Period 2; the fourth row refers to Period 3; and the last row refers to Period 4.

at a specific phase angle, which is linked to the emission local time. Particles detected in the terminator plane are emitted at dawn or dusk from the surface, while particles detected at low phase angles are emitted near local noon. Due to the non-negligible particle traveltime, there is no link between the detection coordinates and the subspacecraft point. The different speed versus mass distributions shown in Fig. 3 are linked to the Sun–zenith angle. The speed increases with decreasing phase angle and heliocentric distance as can be deduced following the evolution of the A parameter (Table 2), which is proportional to the speed. The speed distribution is more shallow with respect to the mass values at phase angles $<75^\circ$, i.e. when the emission areas are illuminated with a small Sun–zenith angle. The values of γ obtained at low phase angles (Table 2) are, within the uncertainties, compatible with 0.167, the value derived for ground-based coma observation interpretation (Fulle 1987). The γ-values obtained for detections collected near the terminator plane (phase angles $>75^\circ$) are about 3–4 times the Fulle (1987) value. Recalling that the cosine of the Sun–zenith angle is considered one of the main drivers modulating the H_2O production rate from the nucleus surface (Fougere et al. 2016), at noon (Sun–zenith angle $= 0^\circ$), the H_2O production rate is at a maximum. We can thus correlate the γ-parameter variability to a difference in the local H_2O production driving dust particle ejection. This is in accordance with other *Rosetta* remote sensing results linking the dust ejection to H_2O production (Migliorini et al. 2016). We have linked the speed versus mass trend parameters with the water production evolution, a function of the heliocentric distance, reported by Fougere et al. (2016) (Fig. 6). The trend of the γ and S_0 parameters (with S_0 being equal to A multiplied by the arbitrary value of $m_0 = 10^{-7}$ kg) with respect to the H_2O global production rate (Fig. 6) is similar to what we find for local illumination conditions (phase angle) linkable to local variability of H_2O production (Fig. 3).

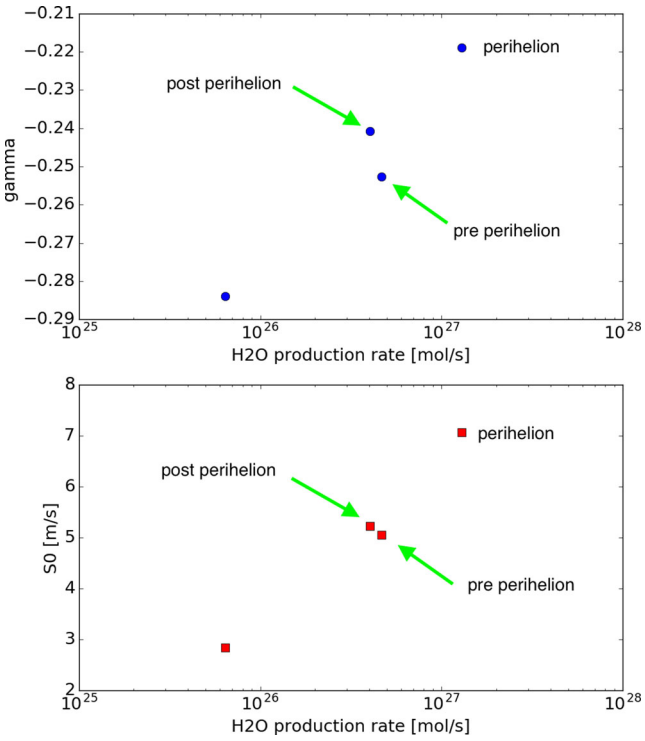

Figure 6. γ and S_0 parameters of the $v = S_0(m/m_0)^\gamma$ equation (with S_0 being equal to A of the obtained fit multiplied by the arbitrary value of $m_0 = 10^{-7}$ kg) estimated for the low phase angle detections as a function of the H_2O production rate given by Fougere et al. (2016). The point corresponding to the lowest production rate refers to the beginning of the *Rosetta* scientific phase (data collected from 2014 August 1 until 2015 January 22). The points indicated by arrows refer to Period 1 (pre-perihelion) and Period 4 (post-perihelion). The point corresponding to the highest production rates refers to Periods 2 and 3 (perihelion).

5 CONCLUSIONS

The analyses of the data collected by GIADA in the period from 2015 January 22 to 2016 February 22 allowed us to study in depth the dust particle distribution in the inner coma. We were able to retrieve five dust density distribution maps showing that most of the dust is concentrated at coordinates in the CSO reference frame corresponding to the most illuminated areas of the nucleus (i.e. low phase angles). The high-density areas in the coma (CSO reference frames) move following the rotation axis, i.e. the comet seasons. The maps show that the major fraction of the dust is emitted at low phase angles, confirming the results reported in Fulle et al. (2016) and Rotundi et al. (2015). This work derived the parameters of the power-law linking particle speeds and their masses, namely A and γ of the equation $v = Am^\gamma$ at different local illumination conditions and heliocentric distances. Analysing how the distribution of the particle speeds versus their mass changes with respect to the observation geometry, i.e. phase angle, and the heliocentric distance, we have derived a global and a local correlation with the H_2O production rate. The proportionality parameter A increases with decreasing heliocentric distance following the increase of the average speed of the particles. The shallower speed distribution found for higher H_2O production rates indicates that for higher cometary activity, particles having significantly different masses have similar speeds.

ACKNOWLEDGEMENTS

GIADA was built by a consortium led by the Universitá degli Studi di Napoli 'Parthenope' and INAF – Osservatorio Astronomico di Capodimonte, in collaboration with the Instituto de Astrofisica de Andalucia, Selex-ES, FI and SENER. GIADA is presently managed and operated by Istituto di Astrofisica e Planetologia Spaziali-INAF, Italy. GIADA was funded and managed by the Agenzia Spaziale Italiana, with the support of the Spanish Ministry of Education and Science Ministerio de Educacion y Ciencias (MEC). GIADA was developed from a Principal Investigator proposal from the University of Kent; science and technology contributions were provided by CISAS, Italy; Laboratoire d'Astrophysique Spatiale, France; and institutions from the UK, Italy, France, Germany and the USA. Science support was provided by NASA through the U.S. *Rosetta* Project managed by the Jet Propulsion Laboratory/California Institute of Technology. We would like to thank A. Coradini for her contribution as a GIADA Co-Investigator. GIADA calibrated data will be available through ESA's Planetary Science Archive (PSA) website (http://www.rssd.esa.int/index.php?project=PSA&page=index). All data presented here are available on request before archiving in the PSA. This research was supported by the Italian Space Agency (ASI) within the ASI-INAF agreements I/032/05/0 and I/024/12/0. We thank the anonymous referees for their helpful critiques that have resulted in significant improvement to the manuscript.

REFERENCES

Crifo J.-F., Rodionov A. V., Szegö K., Fulle M., 2002, Earth Moon Planets, 90, 227

Della Corte V. et al., 2014, J. Astron. Instrum., 3, 1350011
Della Corte V. et al., 2015, A&A, 583, A13
Della Corte V. et al., 2016, Acta Astronaut., 126, 205
Efron B., Tibshirani R. J., 1994, An Introduction to the Bootstrap. CRC Press, New York
Ferrari M., Della Corte V., Rotundi A., Rietmeijer F. J. M., 2014, Planet. Space Sci., 101, 53
Fougere N. et al., 2016, A&A, 588, A134
Fulle M., 1987, A&A, 171, 327
Fulle M. et al., 2015, ApJ, 802, L12
Fulle M. et al., 2016, ApJ, 821, 19
Keller H. U. et al., 1986, Nature, 321, 320
Keller H. U. et al., 2007, Space Sci. Rev., 128, 433
Lara L. M. et al., 2015, A&A, 583, A9
Lin Z.-Y. et al., 2016, A&A, 588, L3
McBride N., Green S. F., Levasseur-Regourd A.-C., Goidet-Devel B., Renard J.-B., 1997, MNRAS, 289, 535
Migliorini A. et al., 2016, A&A, 589, A45
Preusker F. et al., 2015, A&A, 583, A33
Rotundi A. et al., 2015, Science, 347, aaa3905
Vincent J.-B., Lara L. M., Tozzi G. P., Lin Z.-Y., Sierks H., 2013, A&A, 549, A121
Vincent J.-B. et al., 2015, Nat, 523, 63
Zakharov V. V., Rodionov A. V., Lukianov G. A., Crifo J. F., 2009, Icarus, 201, 358

[1]*INAF – Instituto Astrofisica e Planetologia Spaziali, via del Fosso del Cavaliere, 100, Roma I-00133, Italy*
[2]*Dipartimento Scienza e tecnologia, Università degli Studi di Napoli 'Parthenope', Centro Direzionale di Napoli isola C4, Napoli I-80143, Italy*
[3]*INAF – Osservatorio Astronomico di Trieste, Via Tiepolo 11, Trieste I-34143, Italy*
[4]*Planetary and Space Sciences, School of Physical Sciences, The Open University, Milton Keynes MK7 6AA, UK*
[5]*Department of Earth and Planetary Science, MSC 03 2040, 1-University of New Mexico, Albuquerque, NM 87131-0001, USA*
[6]*ESA, European Space Research and Technology Centre (ESTEC), Keplerlaan 1, 2201 AZ Noordwijk, The Netherlands*
[7]*Osservatorio Astronomico Catania, INAF, Via S.Sofia 78, I-95123 Catania, Italy*
[8]*LESIA, Obs. de Paris, CNRS, Univ Paris 06, Univ. Paris-Diderot, 5 place J. Janssen, F-92195 Meudon, France*
[9]*INAF Osservatorio Astronomico di Roma, Via di Frascati, 33, Monte Porzio Catone, Rome, Italy*
[10]*Planetary Science Institute, 1700 E Fort Lowell, Tucson, AZ 85719, USA*
[11]*Max-Planck-Institut fuer Kernphysik, Saupfercheckweg 1, D-69117 Heidelberg, Germany*
[12]*Instituto de Astrofisica de Andalucìa, Consejo Superior de Investigaciones Cientìficas (CSIC), PO Box 3008, E-18080 Granada, Spain*
[13]*Laboratoire Atmosphères, Milieux, Observations Spatiales, CNRS/ Université de Versailles Saint-Quentin-en-Yvelines/Institut Pierre-Simon Laplace, 11 boulevard d'Alembert, F-78280 Guyancourt, France*
[14]*INAF Osservatorio Astronomico di Capodimonte, Salita Moiariello, 16, I-80133 Naples, Italy*
[15]*Laboratoire d'Astrophysique de Marseilles, UMR 7326, CNRS & Aix Marseille Université, F-13388 Marseilles Cedex 13, France*
[16]*The University of Kent, Canterbury, Kent CT2 7NZ, UK*
[17]*UnispaceKent, Canterbury, Kent CT2 8EF, UK*
[18]*Departamento de Fisica Aplicada, Universidad de Granada, Facultad de Ciencias, Avda. Severo Ochoa, s/n, E-18071 Granada, Spain*
[19]*Observatoire de Haute Provence OSU Pythéas UMS 2244 CNRS-AMU, F-04870 Saint Michel l'Observatoire, France*
[20]*Centro de Astrobiologia (INTA-CSIC), E-28691 Villanueva de la Canada, Madrid, Spain*
[21]*International Space Science Institute, Hallerstrasse 6, CH-3012 Bern, Switzerland*
[22]*Leonardo, Via A. Einstein, 35, I-50013 – Campi Bisenzio (Firenze), Italy*
[23]*Virginia Polytechnic Institute and State University, Blacksburg, VA 24061, USA*
[24]*University of Florida, Gainesville, FL-32611, USA*

This paper has been typeset from a TEX/LATEX file prepared by the author.